Combined Primary Frequency and Virtual Inertia Response Control Scheme of Variable-Speed Dish-Stirling System

Citation for the original published paper (version of record):
Li, Y., Choi, S., Vilathgamuwa, D. et al (2020)
Combined Primary Frequency and Virtual Inertia Response Control Scheme of Variable-Speed Dish-Stirling System
IEEE Access, 8: 151719-151730
http://dx.doi.org/10.1109/ACCESS.2020.3017791

IEEE Access
Multidisciplinary ⋮ Rapid Review ⋮ Open Access Journal

Received August 7, 2020, accepted August 16, 2020, date of publication August 19, 2020, date of current version August 28, 2020.

Digital Object Identifier 10.1109/ACCESS.2020.3017791

Combined Primary Frequency and Virtual Inertia Response Control Scheme of a Variable-Speed Dish-Stirling System

YANG LI[1], (Member, IEEE), SAN SHING CHOI[2], D. MAHINDA VILATHGAMUWA[2], (Fellow, IEEE), BINYU XIONG[1], (Member, IEEE), AND JINRUI TANG[1], (Member, IEEE)

[1]School of Automation, Wuhan University of Technology, Wuhan 430072, China
[2]School of Electrical Engineering and Robotics, Queensland University of Technology, Brisbane, QLD 4001, Australia

Corresponding author: Jinrui Tang (tangjinrui@whut.edu.cn)

This work was supported in part by the National Natural Science Foundation of China under Grant 51707139, in part by the National Natural Science Foundation of China under Grant 61703318, and in part by the Fundamental Research Funds for the Central Universities of China under Grant WUT: 203111001.

ABSTRACT The potential of variable-speed dish-Stirling (VSDS) solar-thermal generating plant in providing grid frequency support is investigated. In the proposed VSDS frequency support control scheme, the reference speed of the Stirling engine is regulated to track a deloaded power curve which is governed by the solar insolation level. The gain of a supplementary speed-frequency droop controller is then set to meet the primary frequency control requirement. Further uniqueness of the VSDS control scheme pertains to the provision of virtual inertia response by regulating the kinetic energy in the rotating mass of the engine-generator and the thermal energy in the heat absorber/receivers. Small-signal analysis shows that the frequency support scheme is inherently stable, and it will provide higher degree of damping as the penetration level of the VSDS system and/or the solar insolation level increase. The efficacy of the proposed scheme is validated by computer simulation.

INDEX TERMS Dish-Stirling system, solar-thermal power generation, primary frequency control, virtual inertia response.

I. INTRODUCTION

Global electricity supply systems have undergone unprecedented structural changes due to the ever-increasing penetration of renewable generation, including that of wind and solar. Dish-Stirling (DS) system is one type of solar power generation in which a dish-like reflector concentrates sunlight to a focal point [1] in which an assembly of receiver/absorbers is located. The high-temperature receiver/absorbers become the heat source for a closed-cycle external heat engine, the Stirling engine. This method of sustainable generation is proven to be most efficient amongst the various concentrated solar power technologies [2].

In the past decade or so, the DS system has received much research attention, especially with regard to its modeling, design, and integration into electrical power systems [3]. Castellanos *et al*. [4] propose a mathematical DS model intended for the optimal opto-geometric design of the concentrator and heat receiver, and the model is validated experimentally in [5]. A methodology is developed in [6] using a modified Iwamoto mathematical model of Stirling engine and a solar prediction model to evaluate the performance of a DS system. The authors show that global energy efficiency ranges between 19–26%. Caballero *et al*. [7] investigate a DS system equipped with a directly illumined receiver. Their focus is on the optimization of power output and efficiency, and a detailed model has been developed for the opto-geometric and heat transfer mechanisms in the collector-receiver system. The radiative property of the DS cavity receiver is studied in [8] using experimental and numerical methods, and improved design has been obtained as a result. Novel configurations and co-generations of dish-Stirling systems have also been proposed, with the view to obtain additional benefits such as higher efficiency and

The associate editor coordinating the review of this manuscript and approving it for publication was S. Srivastava.

improved reliability. A free-piston Stirling engine for a combined heating-power generation system has been developed and is reported to have achieved the overall energy conversion efficiency of 38.25% [9]. Furthermore, DS integrated with high-temperature superconducting linear generator has been proposed and analyzed in [10], and it shows high potential for large-scale application of solar power generation system. To maximize the solar energy harness, variable-speed doubly-fed induction generators (DFIGs) have also been proposed for incorporation into the DS systems [11], [12]. Compared to the conventional fixed-speed DS systems (FSDS) and depending on the weather condition, typically some 4%–11% increase in the energy harness can be expected through the adjustments in the operating speed of the Stirling engines/generators. The authors of [13] propose the use of permanent magnet synchronous generators to achieve variable-speed DS (VSDS) operation so as to provide superior control performance, but cost is a major drawback.

Once DS generation is introduced into a grid, often one performance requirement imposed on it is that it has to provide frequency control ancillary services [14]. While the economic benefit of the increased energy harness using the VSDS system reported in [11] would be negated somewhat by the cost of the power converter which makes the variable speed operations possible, nevertheless, the VSDS generator permits the independent control of the real and reactive power flows at its terminals. This flexibility allows for the stipulated frequency and voltage controls, a performance that is essential to ensure the successful integration of large-scale DS power generation into grid systems [15]. Indeed, recent works [16]–[19] focus specifically on the hybridization of multi-source and energy storage to provide frequency support. These works utilize relatively simple DS models in their studies and do not consider the thermodynamic limits placed on the prime mover of the DS system, i.e., the Stirling engine. In general, a grid-connected generator is to adjust its output power in response to grid system frequency variations, if the generator is to provide primary frequency support. Wind turbine generators (WTG) can assume this role through the deliberate de-loading of its operating point from the theoretical maximum power point tracking locus. The de-loading can be realized either from speed control [20], prime mover control (pitch control), or the combination of the two [21], [22]. However, the power converter in modern WTG decouples the rotating mechanical system of the generator from the electrical grid system, with the result that the system inertia is less than that if a synchronous generating unit of the same capacity is used instead. A low inertia system tends to result in a larger excursion of the grid frequency following a disturbance. Hence, there have been various attempts to design virtual inertia response (VIR) algorithms by making use of the stored kinetic energy in the rotating mass of the WTG to emulate the conventional inertia so that the rate of change of frequency (ROCOF) can be effectively reduced in the first few seconds following the disturbance [23]. The VIR control schemes are designed for both interconnected ac/dc systems [24], multi-terminal dc system [25], and microgrid systems [26]–[29], utilizing different control schemes such as H-infinity control [27], derivative control [28], fuzzy-logic control [29], among others. Unfortunately, these VIR controller designs are not applicable for the DS system because the prime mover (the turbine) of a wind generator operates on a completely different principle from that of the Stirling engine in a VSDS generating system. The present work also differs from [30] in which the power flow control on the Stirling engine of a fixed-speed DS system is achieved by varying the operating temperature of the absorber/receivers. On the other hand, in the VSDS system investigated in the present work, rather than adjusting the temperature, the focus will be on varying the engine/generator speed while attempting to maintain the receiver/absorbers temperature close to its maximum value. To the best knowledge of the authors, this would be the first reported work investigating the thermodynamic characteristics of the VSDS and from which, a coordinated control scheme based on the speed and temperature of the VSDS has been developed, with the aim to explore the potential of primary frequency support and VIR offered by the VSDS system.

In view of the above, the major contributions of the present investigation are, first, by taking into consideration the practical operational constraints placed on the VSDS system, the extent of its ability to provide primary frequency support for the grid system is identified. Suitable deloaded power tracking curve is determined to meet the reserve power requirement as specified in grid codes, and from which a droop controller is designed to regulate the output power of the generator. Second, for the first time, the capability of the VSDS system to provide VIR is analyzed. The inertia response is achieved by controlling the amount of the stored kinetic and thermal energies contained in the prime mover, the electric generator, and the receiver/absorbers. Third, through a detailed analysis, it is determined that the proposed VSDS frequency support scheme is inherently stable. The VSDS system provides higher degree of system damping as the VSDS penetration level and/or the solar insolation level increase. This characteristic therefore augurs well for the case of high penetration of VSDS generation into utility grid or microgrid systems.

Details of the above three contributions are given in Sections II, III, and IV, respectively. Illustrative examples are provided in Section V while the main findings are summarized in Section VI.

II. PRIMARY FREQUENCY CONTROL OF VSDS SYSTEM

In this section, the feasible operating zone of the VSDS system shall be determined using a developed dynamic model of the system, following which the deloaded operating curve of the DS system is derived. Primary frequency support is then shown to be achievable by the control actions of a speed-frequency droop controller.

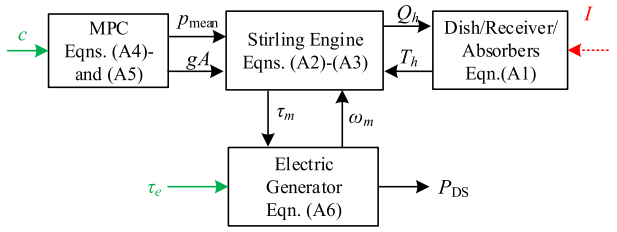

FIGURE 1. Block diagram of the VSDS plant model.

A. FEASIBLE OPERATING ZONE OF THE VSDS SYSTEM

As shown in Fig. 1, the VSDS system under investigation features four sub-systems [31]: 1) a heat collection system consisting of a parabolic dish, a receiver, and absorbers; 2) a double-acting kinematic Stirling engine; 3) a variable-speed electric generator, and 4) a mean pressure control (MPC) system. Its system-level model was developed in [11], [32], where the accuracy of the model had been verified by comparing the simulation results obtained using this model with those yielded by a high-order benchmark model derived based on thermodynamics principles. The complexity of the model is compatible with the purpose of the present study on frequency control. The model is recapitulated in Appendix A as (A1)–(A6).

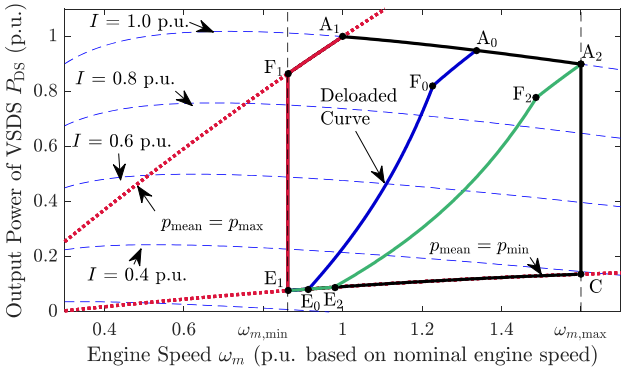

FIGURE 2. Feasible operating zone and tracking curve for primary frequency control derived at the maximum receiver temperature $T_h = 1$ p.u. The boundaries are represented by 1) A_1–F_1: the maximum mean gas pressure $p_{\text{mean}} = p_{\max}$; 2) C–$E_1$: the minimum mean gas pressure $p_{\text{mean}} = p_{\min}$; 3) A_1–A_2: the maximum solar insolation $I = 1.0$ p.u; 4) A_2–C the maximum engine speed $\omega_m = \omega_{m,max}$; and 5) F_1–E_1 the minimum engine speed $\omega_m = \omega_{m,min}$.

By setting the time derivative terms of the state variables (i.e., the receiver temperature T_h, the mean gas pressure p_{mean}, the net mass flow rate gA of the working gas, and the engine speed ω_m) to zero in (A1)–(A6), and following the procedure presented in [11], the steady-state relationship governing the DS output power P_{DS} and the engine speed ω_m at constant temperature can be obtained. This relationship is depicted in Fig. 2 in the form of several equal-insolation curves for a range of solar insolation level I. The steady-state feasible operating zone (FOZ) of the VSDS system, prescribed by the boundary $A_1A_2CE_1F_1A_1$, is obtained by superimposing various P_{DS} vs. ω_m boundary curves onto Fig. 2. These boundary curves are derived to meet practical limits placed on ω_m, p_{mean}, and I, as shown. For the purpose of frequency regulation, the VSDS system shall operate within the FOZ to avoid physical damage to the devices. The nominal operating point for primary frequency control shall be determined based on the FOZ and grid code requirements, as discussed next.

B. DELOADED TRACKING

As explained earlier in the Introduction section, the provision for grid frequency support is usually stipulated for non-synchronous grid-connected generating units [33]. For example, the Spanish grid code on primary frequency control imposes a speed droop requirement of between 2% to 6.66% and the maximum response time of 15 s on generating units [14]. The droop setting is specified so that the appropriate amount of the upward reserve power is available from the units to provide primary frequency support following an under-frequency event, i.e. when the grid frequency f is below 1 p.u. A downward reserve power margin is likewise specified to provide the support following an over-frequency ($f > 1$ p.u.) event.

To simplify the analysis, it is assumed that the same droop setting of $x\%$ is specified for both the upward and the downward reserve powers and the presence of dead band is not considered. From Fig. 2, it can be seen that P_{DS} on the boundary $A_1F_1E_1$ corresponds to the maximum feasible VSDS output power at given I. For conventional operations, it is expected that the VSDS system tracks this curve to ensure the maximum energy harness. In order to provide sufficient primary frequency reserve, this maximum power is to include the $+x\%$ upward reserve power in addition to the P_{DS} described by the curve $A_0F_0E_0$, where $A_0F_0E_0$ determines the desired deloaded operating states of the VSDS system when the grid frequency is at its nominal value ($f_0 = 1$ p.u.). Furthermore, $A_2F_2E_2$ would be the P_{DS} vs. ω_m curve where the P_{DS} is to include the $-x\%$ downward reserve power from that prescribed by $A_0F_0E_0$.

Fig. 3(a) shows the ω_m vs. I relationships which correspond to that with the $+x\%$ reserve, $-x\%$ reserve, and the nominal deloaded operations. The governing functions are denoted as $\omega_{m1}(I)$, $\omega_{m2}(I)$, and $\omega_{m0}(I)$ respectively. Similarly, the corresponding P_{DS} vs. I relationships are denoted by functions $P_{\text{DS1}}(I)$, $P_{\text{DS2}}(I)$, and $P_{\text{DS0}}(I)$, respectively in Fig. 3(b). These functions will be used later in the design of the droop controller for primary frequency support.

As I varies and at the nominal grid frequency, $\omega_{m0}(I)$ and $P_{\text{DS0}}(I)$ track the steady-state speed and output power of the VSDS system. The *Deloaded Tracking* block in Fig. 4 determines the nominal operating engine speed $\omega_{m0}(I)$ at the given I, in accordance to the tracking curve $A_0F_0E_0$. On the other hand, $\omega_{m1}(I)$, $\omega_{m2}(I)$, $P_{\text{DS1}}(I)$, and $P_{\text{DS2}}(I)$ prescribe the bounds on the steady-state ω_m and P_{DS}. The bounds are obtained in order to meet the specified speed droop requirement, as considered in the next sub-section.

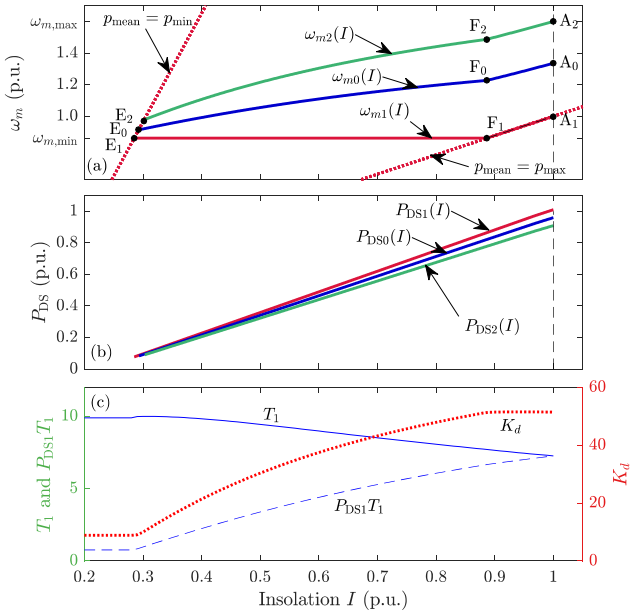

FIGURE 3. Steady-state relationships of (a) ω_m vs. I; (b) P_{DS} vs. I; and (c) T_1, $P_{DS1}T_1$, K_d with I.

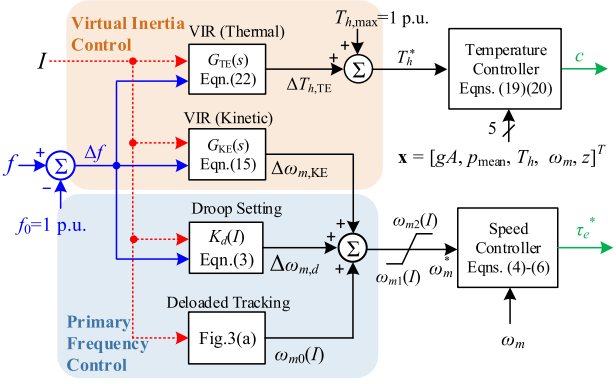

FIGURE 4. Block diagram of the proposed VSDS system primary frequency and inertia response control scheme. The insolation I is assumed to vary much slower than the frequency perturbation.

C. DROOP SETTING

Consider an under-frequency event such that f decreases below 1 p.u. As the dynamics for primary frequency control typically lasts for 10−20 s, the insolation level I can be considered constant over the duration of the event. This quasi-static assumption will be applied for the rest of the analysis. Thus, the VSDS operating state shall move along the respective equal-insolation curve, from the point on the deloaded curve $A_0F_0E_0$ towards that on the maximum power curve $A_1F_1E_1$. In response to the frequency deviation $\Delta f = f - f_0$, it is now proposed the primary frequency support is to be realized by adding a supplementary control action which results in a change $\Delta\omega_{m,d}$ on the engine speed such that

$$\Delta\omega_{m,d} = K_d \Delta f \tag{1}$$

where K_d is the gain of the droop controller. As shown in Fig. 4, the supplementary signal $\Delta\omega_{m,d}$ is added to $\omega_{m0}(I)$ as one constituent input in constructing the set-point ω_m^* of the engine speed controller. K_d shall be set in such a way that P_{DS} is increased by the amount of accelerating power equals to $x\%$ of $P_{DS1}(I)$, from the nominal level $P_{DS0}(I)$, when f decreases by an amount Δf_{max}. Δf_{max} is a design parameter and it may be set as the maximum allowable frequency drop before the onset of under-frequency load shedding. In this manner, the VSDS system is to increase P_{DS} using the upward reserve power and thus helps to prevent the load-shedding from occurring. Accordingly, the constant droop, which is denoted as R_{DS} and governs the change in grid frequency f in response to the change in the VSDS system output power P_{DS}, can be expressed as

$$R_{DS} = \frac{\Delta f_{max}}{x\%} = \frac{\Delta f_{max}}{\frac{P_{DS1}(I) - P_{DS0}(I)}{P_{DS1}(I)}} = -\frac{\Delta f}{\Delta P_{DS}} P_{DS1}(I) \tag{2}$$

Using (1) and (2), one obtains K_d as a function of I, i.e.,

$$K_d(I) = \frac{\Delta\omega_{m,d}}{\Delta f} = \frac{\Delta\omega_m}{\Delta P_{DS}} \frac{\Delta P_{DS}}{\Delta f} \approx -\frac{\partial\omega_m}{\partial P_{DS}} \frac{x\%}{\Delta f_{max}} P_{DS1}(I) \tag{3}$$

where $\partial\omega_m/\partial P_{DS} \approx \Delta\omega_m/\Delta P_{DS}$ is the reciprocal of the gradient of the deloaded tracking curve $A_0F_0E_0$ at the given I. Hence, K_d has to be adaptively adjusted in accordance to the insolation level to meet the constant droop setting requirement. This is indicated in the *Droop Setting* block in Fig. 4, based on the K_d vs. I relationship shown in Fig. 4(c).

Similar reasoning also applies in the case of over-frequency whereby P_{DS} will be reduced by the amount of decelerating power equals to $x\%$ of $P_{DS1}(I)$ when the frequency increases by Δf_{max}. The operating point shall move toward $A_2F_2E_2$ in this instance. The detail is not discussed in this work for the sake of brevity.

D. ANALYSIS OF THE DYNAMIC PERFORMANCE OF PRIMARY FREQUENCY CONTROLLER UNDER ENGINE SPEED CONTROL

As alluded to in Section II-B, apart from the droop requirement, response time is also stipulated in grid codes for primary frequency support. The dynamics of the proposed primary control scheme can now be investigated using small-signal analysis.

The response characteristics of the proposed primary frequency control scheme are governed by the speed feedback which dynamically tracks the speed set-point ω_m^* as I varies:

$$\dot{z}(t) = K_{I,\omega}\left[\omega_m(t) - \omega_m^*(t)\right] \tag{4}$$

$$\tau_e(t) = K_{P,\omega}\left[\omega_m(t) - \omega_m^*(t)\right] + z(t) + D_a\omega_m(t) \tag{5}$$

Here $K_{P,\omega}$, $K_{I,\omega}$, D_a, and z are the proportional gain, integral gain, the active damping constant, and the integrator output of the speed controller respectively. Such a feedback scheme determines the electromagnetic torque τ_e of the generator and can effectively reject disturbances appearing in the mechanical torque τ_m emanating from the prime mover, including those due to the temperature control action [11]. The parameter settings of the speed regulator in (4) and (5)

can be tuned by adopting the internal model control method based on the desired rise time t_{rise}, i.e.,

$$K_{P,\omega} = 2H_m\alpha_\omega \tag{6a}$$
$$K_{I,\omega} = 2H_m\alpha_\omega^2 \tag{6b}$$
$$D_a = K_{P,\omega} - D_m \tag{6c}$$

where H_m is the inertia constant of the rotating mass and $\alpha_\omega = \ln 9/t_{\text{rise}}$ is the desired bandwidth of the speed control loop. D_m is the equivalent damping constant and it can be expressed as a function of insolation I, i.e.,

$$D_m(I) = -\left.\frac{\Delta\tau_m(s)}{\Delta\omega_m(s)}\right|_{s=0} = \frac{K_{\text{mp}}(I)K_{\text{hw}}(I)}{K_{\text{hp}}(I)} - K_{\text{mw}}(I) \tag{6d}$$

where $K_{\text{hp}} = \partial Q_h/\partial p_{\text{mean}}$, $K_{\text{hw}} = \partial Q_h/\partial\omega_m$, $K_{\text{mp}} = \partial\tau_m/\partial\omega_m$, $K_{\text{mw}} = \partial\omega_m/\partial\omega_m$. The derivation of (6d) is provided in Section I of the Supplementary Materials, while the expressions of K_{hp}, K_{hw}, K_{mp} and K_{mw} are given in Appendix B.

Using (A6) and (4)–(6), one can derive the transfer function between P_{DS} and ω_m^* as (see Section II of the Supplementary Materials for details)

$$\frac{\Delta P_{\text{DS}}(s)}{\Delta\omega_m^*(s)} = -\frac{2H_m\omega_{m0}}{T_1}\frac{T_1 s+1}{T_2 s+1} \tag{7}$$

where the time constants are expressed as

$$T_1(I) = \frac{2H_m}{D_m(I) - \tau_{e0}(I)/\omega_{m0}(I)} \tag{8a}$$
$$T_2 = 1/\alpha_\omega \tag{8b}$$

Next, under the droop setting scheme (3) and using (7), one obtains the transfer function between the generated power and the system frequency, viz.,

$$\frac{\Delta P_{\text{DS}}(s)}{\Delta f(s)} = \frac{\Delta P_{\text{DS}}(s)}{\Delta\omega_m^*(s)}\frac{\Delta\omega_{m,d}(s)}{\Delta f(s)} = -\frac{2H_m\omega_{m0}K_d}{T_1}\frac{T_1 s+1}{T_2 s+1} \tag{9}$$

The transfer function (9) governs the small-signal dynamic behavior of the VSDS system under the speed control mode. The steady-state gain of (9) represents the droop $1/R'_{\text{DS}}$ defined based on the rating of the VSDS system. With (2) and (9), $1/R'_{\text{DS}}$ can be expressed as,

$$\frac{1}{R'_{\text{DS}}} = \frac{2H_m\omega_{m0}K_d}{T_1} = -\left.\frac{\Delta P_{\text{DS}}(s)}{\Delta f(s)}\right|_{s=0} \approx \frac{\Delta P_{\text{DS}}}{\Delta f} = \frac{P_{\text{DS1}}(I)}{R_{\text{DS}}} \tag{10}$$

As shown in Fig. 3(b), $P_{\text{DS1}}(I)$ is an increasing function and so the steady-state gain of the proposed primary frequency droop control scheme (1) increases with the insolation.

Also, (8b) shows that once the desired bandwidth α_ω has been specified, T_2 will be determined. Hence, the position of the pole of (9) will be independent of I. On the other hand, the zero of the transfer function is $-1/T_1$ and from (8a). T_1 is shown to be proportional to the inertia constant H_m and is also a function of I. In Appendix B, it proves that T_1 is positive for all I. Therefore, the primary frequency control loop is a minimum-phase system. The relationship between T_1 and I displayed in Fig. 3(c) indicates that T_1 tends to increase as I decreases. Therefore, the step response of the speed control loop will show increasingly larger overshoots/undershoots in P_{DS} as the insolation level decreases. If the overshoot/undershoot is excessive, there are well-established compensation techniques that could be used to enhance the dynamic response of the speed control loop.

Having analyzed how the control of the engine speed can impact the primary frequency support, the next task is to examine how the speed change could be coupled to the inertia responses of the VSDS system which then leads to the complete primary frequency control scheme shown in Fig. 4.

III. VIRTUAL INERTIA RESPONSE OF VSDS SYSTEM

A. VIRTUAL INERTIA RESPONSE USING KINETIC ENERGY

The kinetic energy (KE) stored in the rotating mass of a synchronous generator (SG) and the coupled prime mover tends to reduce the ROCOF in the initial few seconds following a generation-load imbalance. This process is referred to as the inertia response [34]. For the DS system in which the engine/generator operates at the initial rotor speed of ω_{m0}, a rotor speed change of $\Delta\omega_m$ will produce a change in the KE by the amount

$$\Delta E_{\text{KE}} = H_m(2\omega_{m0}\Delta\omega_m + \Delta\omega_m^2) \tag{11}$$

Note that the unit of energy is per unit power times second (p.u. ×s) in this work. From the $\omega_{m1}(I)$, $\omega_{m2}(I)$, and $\omega_{m0}(I)$ curves shown in Fig. 3(a), it is noted that under an over-frequency event, the maximum allowable increase in the rotor speed is $\Delta\omega_m = \omega_{m2} - \omega_{m0}$. Hence, the maximum amount of kinetic energy that can be absorbed by the VSDS system is determined by substituting this maximum speed increase value into (11). Conversely, the maximum amount of kinetic energy that can be released by the DS system under an under-frequency condition is obtained by substituting the maximum allowable speed decrease value $\Delta\omega_m = \omega_{m1} - \omega_{m0}$ into (11). Fig. 5 shows the maximum amounts of the kinetic energy ΔE_{KE} available to provide the VIR support, plotted against the isolation level I when $H_m = 0.5$ s. To determine the corresponding maximum duration for which the VIR can be supported, divide the maximum ΔE_{KE} by the VSDS decelerating or accelerating power during an over-frequency or under-frequency event, respectively. For example, Fig. 5 shows that at $I = 0.7$ p.u., the maximum ΔE_{KE} are 0.281 p.u. ×s (absorbing) and 0.298 p.u. ×s (releasing). If 0.1 p.u. power is demanded for the VIR support, the maximum durations are 2.81 s and 2.98 s for the over-frequency and under-frequency VIR support, respectively.

Based on the definition given in [35], the inertia constant of such a non-synchronous generating system is defined as

$$H_{\text{IR}} = -\frac{1}{2}\frac{\Delta P_{\text{DS}}(s)}{s\Delta f(s)} \tag{12}$$

The speed control scheme described in Section II-D decouples the mechanical system from the electrical system. So the

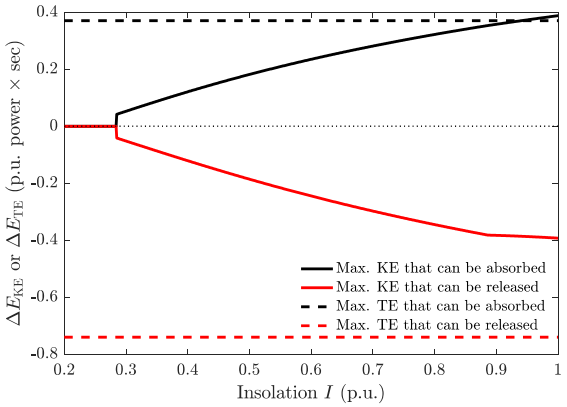

FIGURE 5. Relationship between the insolation level, the maximum available kinetic energy, and thermal energy that can be released or absorbed by the VSDS system for VIR support. Energy absorbed under the over-frequency condition is shown as positive, and energy released under the under-frequency condition is shown as negative.

KE in the rotor mass of a variable-speed generator-based system cannot respond to any variation in f when such a speed control scheme is used [36]. To overcome this shortcoming, a supplementary control action is now proposed by implementing the KE control block shown in Fig. 4. It is to provide the KE VIR expressed by

$$G_{\mathrm{KE}}(s) = \frac{\Delta\omega_{m,\mathrm{KE}}(s)}{\Delta f(s)} \tag{13}$$

$G_{\mathrm{KE}}(s)$ will generate the signal $\Delta\omega_{m,\mathrm{KE}}$ based on Δf so as to adjust the speed set-point ω_m^*. The design objective is to emulate the action of a SG such that the VSDS system shall have the virtual inertia constant H_{KE}. From the definition of (12), therefore

$$H_{\mathrm{KE}} = -\frac{1}{2}\frac{\Delta P_{\mathrm{DS}}(s)}{s\Delta f(s)} = -\frac{1}{2}\frac{\Delta P_{\mathrm{DS}}(s)}{\Delta\omega_m^*(s)}\frac{G_{\mathrm{KE}}(s)}{s} \tag{14}$$

Substituting $\Delta P_{\mathrm{DS}}/\Delta\omega_m^*$ in (7) into (14), thus

$$G_{\mathrm{KE}}(s) = \frac{\Delta\omega_{m,\mathrm{KE}}(s)}{\Delta f(s)} = \frac{H_{\mathrm{KE}}}{H_m}\frac{T_1}{\omega_{m0}}\frac{T_2 s+1}{T_1 s+1}s \tag{15}$$

To realize $G_{\mathrm{KE}}(s)$, the pure derivative term in (15) is approximated by the transfer function $s/(Ts+1)$ where T has a suitably selected value.

From (15), it can be seen that for a given H_{KE} and Δf, a VSDS system with a larger H_m will result in smaller speed deviation and thus imposes lesser stress on the shaft system. A similar scheme has been proposed to enable DFIG-based WTG to provide mechanical inertia response. A typical WTG has relatively large H_m due to the connected turbine blades. On the other hand, the Stirling engine is a reciprocating engine and has a small rotating mass. Indeed, a flywheel is often coupled to the engine to increase H_m which in turn results in a smoother output power [37].

B. VIRTUAL INERTIA RESPONSE USING THERMAL ENERGY

It is generally recognized that the stored thermal energy (TE) in most types of concentrated solar power plants can be used to provide VIR in support of grid frequency [38]. For the VSDS system, the change ΔE_{TE} in the TE due to a change ΔT_h in the temperature of the receiver/absorbers is proportional to the thermal capacity C_t, i.e.,

$$\Delta E_{\mathrm{TE}} = C_t \Delta T_h \tag{16}$$

C_t represents the thermal capacity of the receiver as defined in Appendix A.

When an under-frequency situation arises, the receiver/absorbers temperature is to reduce so that some of the stored TE can be released to provide the grid frequency support. Suppose ΔT_h is allowed to reduce by 100 K, i.e., $\Delta T_h = -0.097$ p.u. on the maximum temperature $T_{h,\max}$ base of 1033 K, then from (16), the amount of ΔE_{TE} which can be released is –0.74 p.u. ×s when C_t is 7.652 p.u., as given in Appendix B. Conversely, under an over-frequency condition, the receiver/absorbers would be able to absorb more thermal energy if T_h is permitted to increase. The TE absorption capacity of the receiver would depend on the over-heating tolerance characteristics of the material used for the receiver. For example, if the receiver can withstand a 50 K ($\Delta T_h = 0.048$ p.u.) increase in temperature for up to 5.0 s, again from (16), ΔE_{TE} is 0.377. In contrast to ΔE_{KE}, ΔE_{TE} is not affected by the insolation level. As shown in Fig. 5, it is clear that under most insolation conditions when $I < 0.93$ p.u., ΔE_{TE} is more than ΔE_{KE}, the KE available for use in VIR. Due to these factors, it is clear the VSDS system has significant advantages over those generating systems which have only the stored KE to provide the inertia response.

The TE virtual inertial control block in Fig. 4 is given by

$$G_{\mathrm{TE}}(s) = \Delta T_{h,\mathrm{TE}}(s)/\Delta f(s) \tag{17}$$

As indicated in Fig. 4, this control block will regulate the temperature set-point T_h^* as the frequency varies. Consistent with the definition (12), the virtual inertia constant provided by the stored TE is

$$H_{\mathrm{TE}} = -\frac{1}{2}\frac{\Delta P_{\mathrm{DS}}(s)}{s\Delta f(s)} = -\frac{1}{2}\frac{\Delta P_{\mathrm{DS}}(s)}{\Delta T_h^*(s)}\frac{G_{\mathrm{TE}}(s)}{s} \tag{18}$$

To regulate the temperature, a Takagi–Sugeno fuzzy supervisory controller is used in a manner similar to that described in [11]:

$$c^{(i)}(t) = -\mathbf{K}_1^{(i)}\Delta\mathbf{x}^{(i)}(t) - K_2^{(i)}\int (T_h(t) - T_h^*)dt \tag{19}$$

$$c(t) = \sum_{i\in\{\mathrm{low,medium,high}\}} \mu^{(i)}(I)c^{(i)}(t) \tag{20}$$

Here, three local temperature controllers are designed using the pole-placement method at selected low, medium, and high insolation levels. The state vector is augmented by incorporating the speed controller state z in (4), so that

the state variable $\mathbf{x} = [gA, p_{\text{mean}}, T_h, \omega_m, z]^{\text{T}}$ while i is the index for the ith local controller. For each local controller, $\mathbf{K}_1 = [K_{11}, K_{12}, K_{13}, K_{14}, K_{15}]$ and K_2 constitute the six gain parameters of the state feedback and integral control loops respectively. μ is a membership function of the insolation I determined by the fuzzy supervisor. More detailed explanations including the design of the membership function μ of this temperature control scheme can be found in [11].

Following the detail derivation in Section III of the Supplementary Materials, the transfer function between T_h^* and P_{DS} can be obtained as

$$\frac{\Delta P_{\text{DS}}(s)}{\Delta T_h^*(s)} = \frac{\Delta P_{\text{DS}}(s)}{\Delta T_{h,\text{TE}}(s)} = -\frac{K_{\text{mp}} C_t \omega_{m0}}{K_{\text{hp}}} \frac{(2\alpha_\omega - 1/T_1)s^2 + \alpha_\omega^2 s}{(s+\alpha_\omega)^2} \tag{21}$$

Using (18) and (21), we obtain

$$G_{\text{TE}}(s) = \frac{\Delta T_{h,\text{TE}}(s)}{\Delta f(s)} = \frac{2H_{\text{TE}}}{\omega_{m0} C_t} \frac{K_{\text{hp}}}{K_{\text{mp}}} \frac{(s+\alpha_\omega)^2}{(2\alpha_\omega - 1/T_1)s + \alpha_\omega^2} \tag{22}$$

This VIR using the stored TE will assist in frequency support in the following way. Consider a sudden decrease in f. From (22), $\Delta T_{h,\text{TE}} < 0$ and thus the temperature set-point T_h^* is reduced. As I is unlikely to vary appreciably over such a short period, according to (A1), the only way to reduce T_h is to increase the heat transfer rate Q_h. As Q_h is approximately proportional to p_{mean}, the MPC system will send the valve command c to inject the working gas from a high-pressure tank to the engine cylinder to increase p_{mean}. As the engine power P_m is also approximately proportional to p_{mean}, P_m will increase accordingly. In this way, the VSDS system shall provide the frequency support. Conversely, when f increases, T_h^* increases and the working gas in the cylinder will be dumped to a low-pressure tank. Hence, p_{mean} and thus P_m are reduced. The VSDS system shall therefore reduce the increase in f.

IV. CONTRIBUTIONS TO GRID FREQUENCY SUPPORT

When a DS system is interconnected into a utility grid or microgrid system, a convenient way to assess the contributions of the DS system to grid frequency support is to analyze the parallel operation of the VSDS and an SG. In such a simplified two-machine power system, the SG is to have the permanent droop setting R_{SG} whereas its governor-turbine system can be represented by the first-order model

$$G_{\text{gt}}(s) = 1/(T_{\text{gt}}s + 1) \tag{23}$$

where T_{gt} is the SG governor–turbine time constant.

The frequency control block diagram of the simplified power system is shown in Fig. 6(a), where H and D are the power system inertia constant and damping constant, respectively. The frequency deviation Δf is the result of the load change ΔP_L. H is calculated based on the system generating capacity $S_{N,\text{tot}} = S_{N,\text{SG}} + S_{N,\text{DS}}$, $S_{N,\text{SG}}$ and $S_{N,\text{DS}}$ being the generating capacities of the SG and VSDS power plants

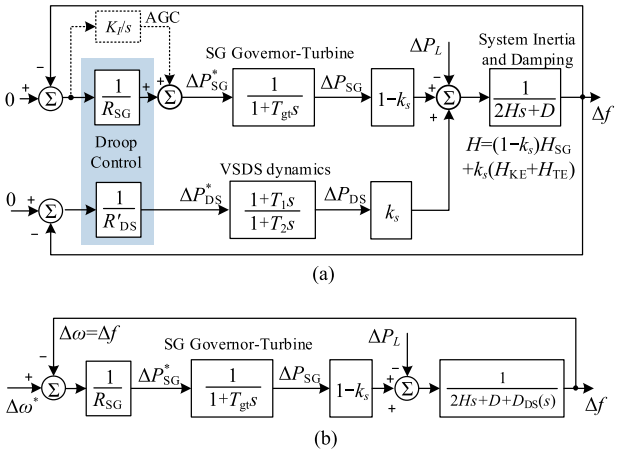

FIGURE 6. Small-signal analysis of the contributions of VSDS in supporting system frequency using (a) a two-machine grid model; (b) the simplified equivalent single-machine model.

respectively, i.e.,

$$H = (1 - k_s)H_{\text{SG}} + k_s(H_{\text{KE}} + H_{\text{TE}}) \tag{24a}$$

$$k_s = S_{N,\text{DS}}/S_{N,\text{tot}} \tag{24b}$$

where k_s represents the penetration level of the VSDS system. Therefore, H depends on the penetration level k_s, the inertia constant H_{SG} of the SG, as well as the virtual inertia constants H_{KE} and H_{TE} of the VSDS system.

In order to study the contributions made by the VSDS system toward primary frequency support, Fig. 6(a) can be converted to Fig. 6(b) where the additional damping term $D_{\text{DS}}(s)$ has been introduced as

$$D_{\text{DS}}(s) = \frac{k_s}{R'_{\text{DS}}} \frac{1 + T_1 s}{1 + T_2 s} \tag{25}$$

Hence, the characteristic equation of the closed-loop transfer function $\Delta f(s)/\Delta\omega^*(s)$ of Fig. 6(b) can be shown to be of the form

$$\Delta(s) = a_3 s^3 + a_2 s^2 + a_1 s + a_0 \tag{26}$$

where it can be readily shown that all the coefficient a_i in (26) as well as $a_2 a_1 - a_3 a_0$ are always positive. As such, the power system is guaranteed to be stable for all VSDS system penetration levels and insolation levels, in accordance to the Routh–Hurwitz criteria. This is an important outcome because it means that with the proposed primary frequency control scheme, VSDS is clearly advantageous over the FSDS system. In [30], it has been shown that instability can occur when the FSDS system operates at high insolation/high penetration levels.

Furthermore, at the initial stage of the frequency transient, the additional damping term D_{DS} is approximately

$$D_{\text{DS}}(s = \infty) = \frac{k_s}{R'_{\text{DS}}} \frac{T_1}{T_2} = k_s \frac{P_{\text{DS1}}(I)}{R_{\text{DS}}} \frac{T_1(I)}{T_2} \tag{27}$$

As $T_1 \gg T_2$ and $R'_{\text{DS}} \ll 1$, the additional damping term introduced by the VSDS system increases with the

penetration level k_s and when R_{DS} decreases, as expected. However, while $P_{DS1}(I)$ and $T_1(I)$ are both functions of the insolation I, Fig. 3(c) shows that the product $P_{DS1}(I)T_1(I)$ increases with I. Therefore, the power system will enjoy higher degree of damping as the insolation level I increases, as k_s, R_{DS} and T_2 are independent of I. So another significant finding of this work is: the increase in damping with the insolation I is a unique characteristic of the proposed VSDS system primary frequency control scheme, a characteristic which is unavailable in the conventional FSDS system.

V. ILLUSTRATIVE EXAMPLES

A. SYSTEM CONFIGURATION

The purpose of using the following examples is to demonstrate the performance of the proposed VSDS primary frequency and VIR control scheme. The two-machine power system analyzed in Section IV is considered suitable for this purpose, because using a more complex multi-machine power system model would introduce many contributing factors and will make it much harder to identify the amount of grid frequency support provided by the VSDS system.

The power system is studied under the MATLAB/Simulink environment. Although the equivalent SG model shown in Fig. 6 is adopted in the simulation, a more detailed SG model such as that described in [39] could be used, if desired. As for the VSDS system, the nonlinear VSDS model contained in Appendix A and the frequency control scheme shown in Fig. 1 are adopted. The total system capacity $P_{N,\text{tot}}$ is 100 MW, and the initial load P_L is 70 MW. At the initial insolation level of 0.8 p.u., according to the $P_{DS0}(I)$ and $P_{DS1}(I)$ curves in Fig. 3(b), the deloaded power and the maximum power are 0.7034 p.u. and 0.7555 p.u. on the VSDS plant rating base of $P_{N,DS}$. Using (3), the frequency–speed droop constant K_d is calculated to be 49.3. The maximum frequency deviation setting $\Delta f_{\max}$ is assumed to be 0.01 p.u. or 0.5 Hz on 50-Hz base. The initial output powers of the SG and the VSDS system depend on the penetration level k_s of the VSDS system. As mentioned earlier, the developed VSDS plant model has been compared with established DS models in [11] and was found to be satisfactory. Hence, the results of the validation of the VSDS plant model shall not be repeated here. The model and control parameters used in the studies are given in Appendix B.

B. CASE 1: VSDS SYSTEM UNDER DROOP CONTROL

The capability of the proposed VSDS speed regulation scheme to provide primary frequency support will be examined, but only under the droop control mode in this case. The VIR schemes proposed in Section III shall be studied in Section V-D. The combined effects of VIR and primary frequency control will also be shown there. A step load increase ΔP_L of 10 MW (0.1 p.u.) is introduced to initiate a frequency disturbance. Two VSDS penetration levels are investigated.

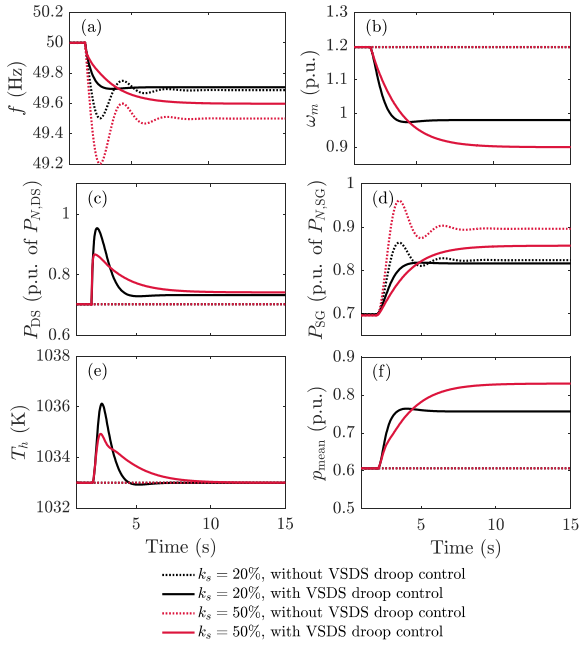

FIGURE 7. Simulation results showing VSDS system with and without droop control, and at 20% and 50% VSDS system penetration levels. Inertia response schemes are not implemented on the VSDS system: (a) system frequency; (b) DFIG angular speed; (c) output power of the VSDS system; (d) output power of the SG; (e) receiver temperature of the VSDS system; (f) mean gas pressure of the VSDS system.

With k_s of 20%, the initial P_{DS} is $100\times0.2\times0.7034$ or 14.07 MW, while P_{SG} is 55.94 MW (0.6992 p.u. of $P_{N,SG}$ of 80 MW). At a higher penetration level k_s of 50%, the initial DS and SG output powers are 35.36 MW and 34.64 MW (0.6928 p.u. on $P_{N,SG}$ of 50 MW base) respectively.

The simulation results with or without the proposed primary frequency droop control are shown in Fig. 7. The post-disturbance steady-state frequency deviation Δf_{ss} shown in the figure can be readily verified using (28):

$$\Delta f_{ss} = -\frac{\Delta P_L}{(1-k_s)/R_{SG} + k_s/R'_{DS}} \tag{28}$$

Without the droop control scheme, the VSDS system clearly does not respond to the frequency decrease. Under this condition, Δf_{ss} for k_s of 20% and 50% are -0.313 Hz and -0.5 Hz respectively. When the proposed frequency droop control is added, the control system attempts to reduce the engine speed to produce more power, as demonstrated in Fig. 7(b) and Fig. 7(c). Δf_{ss} has in turn been reduced to -0.286 Hz and -0.42 Hz for k_s of 20% and 50% respectively. It can be seen from Fig. 7(d) that with the VSDS droop control, the steady-state P_{SG} is less than that when the VSDS system has no droop control: the VSDS system has shared the duty of the primary frequency control with the SG and is consistent with the droop setting.

Regarding the dynamic response, it can also be observed from Fig. 7(a) that the introduction of the droop control has provided much-improved damping to the power system.

It has resulted in the nadir of the frequency excursion curve being raised. This is a desirable outcome because the raised frequency level alleviates the possibility of the occurrence of under-frequency load shedding. Also, the degree of damping is seen to increase with the VSDS penetration level: an observation that is in line with the conclusion drawn from the analysis of Section IV.

Furthermore, Fig. 7(e) shows that the Stirling engine temperature is well-maintained. While during the initial few seconds T_h can be momentarily above its steady-state level, the temperature is rapidly restored, although the duration required to achieve the restoration does increase with k_s.

C. CASE 2: VSDS SYSTEM UNDER DROOP CONTROL AT VARIOUS INSOLATION LEVEL

In this case, the impact of VSDS droop control on the primary frequency support is studied at 0.3 p.u., 0.6 p.u. and 1.0 p.u. insolation levels while k_s is kept at 20%. The initial value of P_{DS} for the three insolation levels are 0.086 p.u., 0.456 p.u., and 0.937 p.u. respectively, before the onset of the same sudden load increase as in Case 1 of 10 MW. The simulation results are shown in Fig. 8.

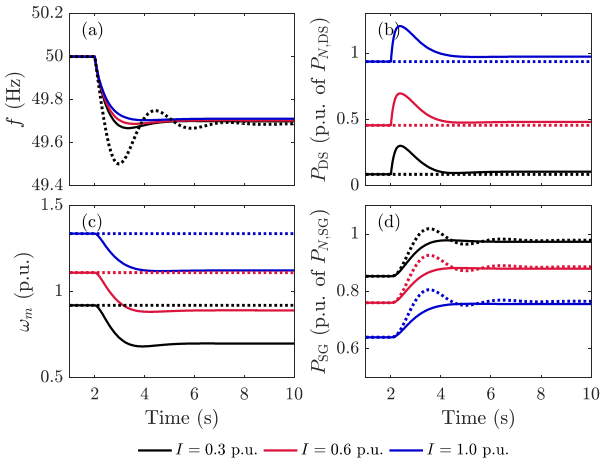

FIGURE 8. Simulation results of VSDS system with (solid lines) and without (dotted lines) droop control under different insolation levels. In all the cases, Inertia response schemes are not implemented on the VSDS system: (a) system frequency; (b) output power of the VSDS system; (c) DFIG angular speed; (d) output power of the SG.

Δf_{ss} can again be verified using (28): when the droop control is applied, Δf_{ss} is -0.3 Hz, -0.297 Hz, -0.281 Hz for the low, medium, and high insolation levels respectively, compared to Δf_{ss} of -0.313 without the droop control. Furthermore, as the insolation level increases, it can be observed from Fig. 8 (a) that the resulting grid frequency excursion is slightly under-damped when the VSDS operates at 0.3 p.u. insolation level and the frequency excursion becomes over-damped when the insolation level is 1 p.u. Hence, this example has once again validated the results of the analysis of Section IV: the VSDS system has provided higher degree of damping to the grid frequency perturbations as the insolation level increases.

D. CASE 3: VSDS SYSTEM WITH VIRTUAL INERTIA RESPONSES

In this case, the efficacy of the VIR schemes considered in Section III will be demonstrated. k_s is still set to 20% and the same load increase as that in Case 1 is assumed. As explained in Section III, the inertia response would only provide frequency support in the first few seconds following the disturbance. Due to the load increase, the steady-state level of f would be below its pre-disturbance value, as in Cases 1 and 2. In this example, this steady-state frequency error is to be eliminated by the automatic generation control (AGC) action. This is realized by adding the integral control block K_I/s in parallel to the droop control of the SG, as shown in Fig. 6.

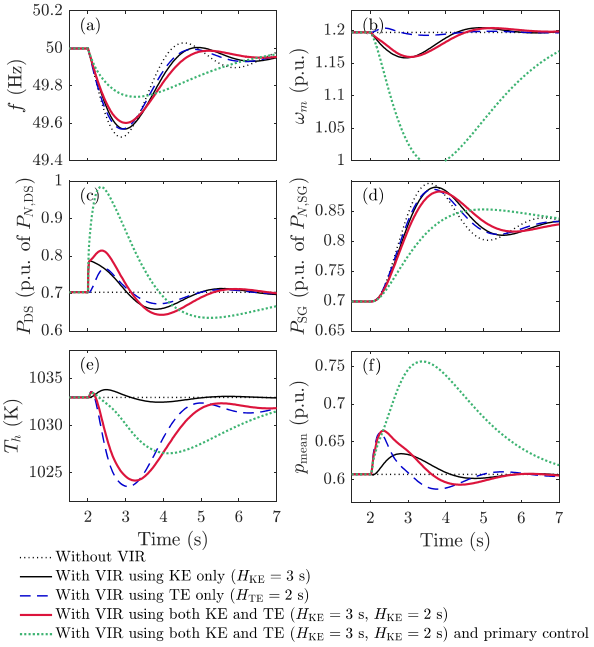

FIGURE 9. Simulation results with different virtual inertia response from VSDS. In all the cases, the SG performs AGC to restore the frequency back to its nominal value: (a) system frequency; (b) DFIG angular speed; (c) output power of the VSDS system; (d) output power of the SG; (e) receiver temperature of the VSDS system; (f) mean gas pressure of the VSDS system.

In order to demonstrate more clearly the impacts of the VIR, the droop control on the VSDS system was omitted first. With $H_{\mathrm{KE}} = 3.0$ s and $H_{\mathrm{TE}} = 2.0$ s, the results of the simulation are as shown in Fig. 9. In Fig. 9(b)–Fig. 9(f), it is not surprising to note that when the inertia responses have not been utilized to provide primary frequency control, the engine speed, receiver temperature, and gas pressure are unaffected by the system frequency variation. With VIR using the stored KE, it can be seen from Fig. 9(b) that the engine speed starts to decrease when f reduces. Thus, KE is released to slow down the frequency decrease. As the SG eventually restores f back to its pre-disturbance level, the released KE will be returned back to the Stirling engine. On the other hand, when VIR from TE only is provided, TE is released and temperature

decreases, as shown in Fig. 9(e). There is a corresponding but rather small speed deviation in this instance, as can be seen in Fig. 9(b). When the KE and TE are used together to provide the VIR, the lowest rate of change of f is observed, and it yields the least amount of the frequency excursion.

Finally, Fig. 9 also shows the combined effects of VIR and primary frequency control. It can be seen that the ROCOF is significantly reduced and system oscillation is effectively damped when primary frequency control is introduced. The reason has been explained in Section IV. Thus, this example has demonstrated the unique beneficial characteristics of the VSDS system which are unavailable in the FSDS system.

VI. CONCLUSION

The potential of variable-speed dish-Stirling (VSDS) solar-thermal generator to provide primary frequency support has been investigated. The proposed variable droop setting scheme to regulate the speed of the Stirling engine is shown to be able to provide the frequency support and meets the grid code reserve power requirement. The virtual inertia response of the VSDS system is utilized to provide additional frequency support for better damping during system disturbance. This is achieved by designing supplementary controllers to utilize the thermal energy stored in the high-temperature receiver/absorbers and the kinetic energy in the rotating mass of the generator/engine. Furthermore, analysis shows that unlike the conventional fixed-speed DS system, the proposed VSDS system frequency control scheme is inherently stable and it provides increased damping as the VSDS system operates under higher insolation level and/or VSDS system penetration level.

APPENDIX A

The VSDS model used in the presented work is developed and validated in [11]. The pertinent equations are

$$T_{\rm rec}\dot{T}_h(t) = K_{\rm rec}\left[K_{\rm con}I(t) - Q_h(t)\right] - \left[T_h(t) - T_a\right] \tag{A1}$$

$$Q_h(t) = \sum_{i=0}^{1}\sum_{j=0}^{1} a_{ij}p_{\rm mean}^{i}(t)\omega_m^{j}(t) + A\left[gA(t)\right] + Cp_{\rm mean}(t)\dot{T}_h(t) \tag{A2}$$

$$P_m(t) = \sum_{i=0}^{1}\sum_{j=0}^{2} b_{ij}p_{\rm mean}^{i}(t)\omega_m^{j}(t) \tag{A3}$$

$$\dot{p}_{\rm mean}(t) = (gA)(t)/K_p \tag{A4}$$

$$T_v\left[g\dot{A}(t)\right] = -(gA)(t) + K_v c(t) \tag{A5}$$

$$2H_m\dot{\omega}_m(t) = \tau_m(t) - \tau_e(t) = \frac{P_m(t)}{\omega_m(t)} - \frac{P_{\rm DS}(t)}{\omega_m(t)} \tag{A6}$$

where T_a is the ambient temperature, $T_{\rm rec}/K_{\rm rec} = C_t$ represents the thermal capacity of the receiver/absorber, Q_h is the heat transfer rate from the receiver to the Stirling engine, a_{ij} and b_{ij} are multivariable polynomial coefficients obtained from engine performance map [11]. The engine power P_m is a function of the mean gas pressure $p_{\rm mean}$ in the engine cylinder and engine speed ω_m. K_p is a gain which describes the linear relationship between $p_{\rm mean}$ and the total mass of the working gas in the engine cylinder, gA is the total mass flow, K_v and T_v are the gain and time constant of the solenoid values, respectively, and c is the command signal sent to the solenoid valves to effect the gas flow. Furthermore, H_m, τ_m, τ_e, and $P_{\rm DS}$ are the inertia constant, mechanical torque, electromagnetic torque, and electromagnetic power, respectively.

APPENDIX B

In this work, ω_{m0}, p_0, τ_{m0}, τ_{e0}, and $P_{\rm DS0}$ represent the values of ω_m, $p_{\rm mean}$, τ_m, τ_e, and $P_{\rm DS}$ at the steady-state operating point when $\Delta f = 0$, respectively. $K_{\rm hp} = a_{10} + a_{11}\omega_{m0}$, $K_{\rm hw} = a_{01} + a_{11}p_0$, $K_{\rm mp} = b_{10}/\omega_{m0} + b_{11} + b_{12}\omega_{m0}$, $K_{\rm mw} = -b_{00}/\omega^{2m0} - b_{10}p_0/\omega^{2m0} + b_{02} + b_{12}p_0$. T_1 is proportional to $(a_{01}/a_{11})(b_{11}\omega_{m0} + b_{12}) - b_{12}(p_0^2/\omega_{m0} + p_0)$. According to the typical parametric values as given below, $a_{01} > 0$, $a_{11} > 0$, $b_{11}\omega_{m0} + b_{12} > 0$, $b_{12} < 0$, and thus it leads to $T_1 > 0$.

Normalized VSDS System Parameters [11]: $a_{00} = 0.045$, $a_{10} = 0.068$, $a_{01} = 0.20$ $a_{11} = 2.14$, $b_{00} = -0.038$, $b_{10} = -0.072$, $b_{01} = 0.055$, $b_{11} = 1.21$, $b_{02} = -0.026$, $b_{12} = -0.13$, $A = -0.2735$, $C = 0.8752$, $K_{\rm con} = 2.865$, $T_{\rm rec} = 13.436$ s, $K_{\rm rec} = 1.756$, $C_t = T_{\rm rec}/K_{\rm rec} = 7.652$, $T_a = 0.288$, $K_v = 1$, $T_v = 0.02$ s, $K_p = 1$, $T_{h,\max} = 1$ p.u., $p_{\max} = 1$ p.u., $p_{\min} = 0.1$ p.u., $\omega_{m,\max} = 1.6$ p.u., $\omega_{m,\min} = 0.8615$ p.u., $H_m = 0.5$ s, $K_{P,\omega} = 3$, $K_{I,\omega} = 9$, $\alpha_\omega = 3$, $x\% = 5\%$, $\Delta f_{\max} = 0.01$ p.u. (0.5 Hz).

Equivalent SG Unit: $H_{\rm SG} = 3.7$, $T_{\rm gt} = 0.5$, $R_{\rm SG} = 0.05$, $K_I = 4.0$, For the description of detailed SG/grid model, readers may refer to [39].

REFERENCES

[1] Y. Li, S. S. Choi, and C. Yang, "Dish-Stirling solar power plants: Modeling, analysis, and control of receiver temperature," *IEEE Trans. Sustain. Energy*, vol. 5, no. 2, pp. 398–407, Apr. 2014.
[2] J. Khan and M. H. Arsalan, "Solar power technologies for sustainable electricity generation—A review," *Renew. Sustain. Energy Rev.*, vol. 55, pp. 414–425, Mar. 2016.
[3] G. Barreto and P. Canhoto, "Modelling of a Stirling engine with parabolic dish for thermal to electric conversion of solar energy," *Energy Convers. Manage.*, vol. 132, pp. 119–135, Jan. 2017.
[4] L. S. M. Castellanos, G. E. C. Caballero, V. R. M. Cobas, E. E. S. Lora, and A. M. M. Reyes, "Mathematical modeling of the geometrical sizing and thermal performance of a Dish/Stirling system for power generation," *Renew. Energy*, vol. 107, pp. 23–35, Jul. 2017.
[5] L. S. M. Castellanos, A. L. G. Noguera, G. E. C. Caballero, A. L. De Souza, V. R. M. Cobas, E. E. S. Lora, and O. J. Venturini, "Experimental analysis and numerical validation of the solar Dish/Stirling system connected to the electric grid," *Renew. Energy*, vol. 135, pp. 259–265, May 2019.
[6] O. R. Sandoval, B. C. Caetano, M. U. Borges, J. J. García, and R. M. Valle, "Modelling, simulation and thermal analysis of a solar dish/Stirling system: A case study in Natal, Brazil," *Energy Convers. Manage.*, vol. 181, pp. 189–201, Feb. 2019.
[7] G. E. C. Caballero, L. S. Mendoza, A. M. Martinez, E. E. Silva, V. R. Melian, O. J. Venturini, and O. A. del Olmo, "Optimization of a dish Stirling system working with DIR-type receiver using multi-objective techniques," *Appl. Energy*, vol. 204, pp. 271–286, Oct. 2017.
[8] J. Garrido, L. Aichmayer, A. Abou-Taouk, and B. Laumert, "Experimental and numerical performance analyses of dish-Stirling cavity receivers: Radiative property study and design," *Energy*, vol. 169, pp. 478–488, Feb. 2019.
[9] S. Zhu, G. Yu, O. Jongmin, T. Xu, Z. Wu, W. Dai, and E. Luo, "Modeling and experimental investigation of a free-piston Stirling engine-based micro-combined heat and power system," *Appl. Energy*, vol. 226, pp. 522–533, Sep. 2018.

[10] Z. Wu and J. X. Jin, "Novel concept of dish Stirling solar power generation designed with a HTS linear generator," *IEEE Trans. Appl. Supercond.*, vol. 24, no. 5, Oct. 2014, Art. no. 5203005.
[11] Y. Li, S. S. Choi, C. Yang, and F. Wei, "Design of variable-speed dish-Stirling solar–thermal power plant for maximum energy harness," *IEEE Trans. Energy Convers.*, vol. 30, no. 1, pp. 394–403, Mar. 2015.
[12] D. Santos-Martin, J. Alonso-Martinez, J. Eloy-Garcia, and S. Arnalte, "Solar dish-Stirling system optimisation with a doubly fed induction generator," *IET Renew. Power Gener.*, vol. 6, no. 4, pp. 276–288, Jul. 2012.
[13] Y. Kadri and H. H. Abdallah, "Performance evaluation of a stand-alone solar dish Stirling system for power generation suitable for off-grid rural electrification," *Energy Convers. Manage.*, vol. 129, pp. 140–156, Dec. 2016.
[14] A. Etxegarai, P. Eguia, E. Torres, A. Iturregi, and V. Valverde, "Review of grid connection requirements for generation assets in weak power grids," *Renew. Sustain. Energy Rev.*, vol. 41, pp. 1501–1514, Jan. 2015.
[15] B. Kroposki, C. Pink, R. DeBlasio, H. Thomas, M. Simões, and P. K. Sen, "Benefits of power electronic interfaces for distributed energy systems," *IEEE Trans. Energy Convers.*, vol. 25, no. 3, pp. 901–908, Sep. 2010.
[16] A. Rahman, L. C. Saikia, and N. Sinha, "Automatic generation control of an interconnected two-area hybrid thermal system considering dish-Stirling solar thermal and wind turbine system," *Renew. Energy*, vol. 105, pp. 41–54, May 2017.
[17] R. Rajbongshi and L. C. Saikia, "Combined voltage and frequency control of a multi-area multisource system incorporating dish-Stirling solar thermal and HVDC link," *IET Renew. Power Gener.*, vol. 12, no. 3, pp. 323–334, Feb. 2018.
[18] W. Tasnin, L. C. Saikia, and M. Raju, "Deregulated AGC of multi-area system incorporating dish-Stirling solar thermal and geothermal power plants using fractional order cascade controller," *Int. J. Electr. Power Energy Syst.*, vol. 101, pp. 60–74, Oct. 2018.
[19] R. Kumar and N. Sinha, "Modeling and control of dish-Stirling solar thermal integrated with PMDC generator optimized by meta-heuristic approach," *IEEE Access*, vol. 8, pp. 26343–26355, Jan. 2020.
[20] G. Ramtharan, J. B. Ekanayake, and N. Jenkins, "Frequency support from doubly fed induction generator wind turbines," *IET Renew. Power Gener.*, vol. 1, no. 1, pp. 3–9, Mar. 2007.
[21] H. T. Ma and B. H. Chowdhury, "Working towards frequency regulation with wind plants: Combined control approaches," *IET Renew. Power Gener.*, vol. 4, no. 4, pp. 308–316, Jul. 2010.
[22] J. Zhao, X. Lyu, Y. Fu, X. Hu, and F. Li, "Coordinated microgrid frequency regulation based on DFIG variable coefficient using virtual inertia and primary frequency control," *IEEE Trans. Energy Convers.*, vol. 31, no. 3, pp. 833–845, Sep. 2016.
[23] Arani and El-Saadany, "Implementing virtual inertia in DFIG-based wind power generation," *IEEE Trans. Power Syst.*, vol. 28, no. 2, pp. 1373–1384, May 2013.
[24] E. Rakhshani and P. Rodriguez, "Inertia emulation in AC/DC interconnected power systems using derivative technique considering frequency measurement effects," *IEEE Trans. Power Syst.*, vol. 32, no. 5, pp. 3338–3351, Sep. 2017.
[25] A. E. Leon, "Short-term frequency regulation and inertia emulation using an MMC-based MTDC system," *IEEE Trans. Power Syst.*, vol. 33, no. 3, pp. 2854–2863, May 2018.
[26] S. Negri, E. Tironi, and D. S. Danna, "Integrated control strategy for islanded operation in smart grids: Virtual inertia and ancillary services," *IEEE Trans. Ind. Appl.*, vol. 55, no. 3, pp. 2401–2411, May/Jun. 2019.
[27] T. Kerdphol, F. S. Rahman, M. Watanabe, and Y. Mitani, "Robust virtual inertia control of a low inertia microgrid considering frequency measurement effects," *IEEE Access*, vol. 7, pp. 57550–57560, Apr. 2019.
[28] T. Kerdphol, F. S. Rahman, M. Watanabe, Y. Mitani, D. Turschner, and H.-P. Beck, "Enhanced virtual inertia control based on derivative technique to emulate simultaneous inertia and damping properties for microgrid frequency regulation," *IEEE Access*, vol. 7, pp. 14422–14433, Jan. 2019.
[29] T. Kerdphol, M. Watanabe, K. Hongesombut, and Y. Mitani, "Self-adaptive virtual inertia control-based fuzzy logic to improve frequency stability of microgrid with high renewable penetration," *IEEE Access*, vol. 7, pp. 76071–76083, Jun. 2019.
[30] Y. Li, S. S. Choi, and D. M. Vilathgamuwa, "Primary frequency control scheme for a fixed-speed dish-Stirling solar–thermal power plant," *IEEE Trans. Power Syst.*, vol. 33, no. 2, pp. 2184–2194, Mar. 2018.
[31] Y. Li, B. Xiong, Y. Su, J. Tang, and Z. Leng, "Particle swarm optimization-based power and temperature control scheme for grid-connected DFIG-based dish-Stirling solar-thermal system," *Energies*, vol. 12, no. 7, p. 1300, Apr. 2019.
[32] Y. Li, S. S. Choi, and C. Yang, "An average-value model of kinematic Stirling engine for the study of variable-speed operations of dish-Stirling solar-thermal generating system," in *Proc. 11th IEEE Int. Conf. Control Autom. (ICCA)*, Jun. 2014, pp. 1310–1315.
[33] J. Matevosyan, T. Ackermann, and S. M. Bolik, "Technical regulations for the interconnection of wind farms to the power system," in *Wind Power in Power Systems*, T. Ackermann, Ed. Hoboken, NJ, USA: Wiley, 2005, pp. 115–142.
[34] E. Ela, M. Milligan, and B. Kirby, "Operating reserves and variable generation," Nat. Renew. Energy Lab., Golden, CO, USA, Tech. Rep. NREL/TP-5500-51978, Aug. 2011.
[35] T. Inoue, H. Taniguchi, Y. Ikeguchi, and K. Yoshida, "Estimation of power system inertia constant and capacity of spinning-reserve support generators using measured frequency transients," *IEEE Trans. Power Syst.*, vol. 12, no. 1, pp. 136–143, Feb. 1997.
[36] J. Ekanayake and N. Jenkins, "Comparison of the response of doubly fed and fixed-speed induction generator wind turbines to changes in network frequency," *IEEE Trans. Energy Convers.*, vol. 19, no. 4, pp. 800–802, Dec. 2004.
[37] C.-H. Cheng and Y.-J. Yu, "Dynamic simulation of a beta-type Stirling engine with cam-drive mechanism via the combination of the thermodynamic and dynamic models," *Renew. Energy*, vol. 36, no. 2, pp. 714–725, Feb. 2011.
[38] P. Denholm, E. Ela, B. Kirby, and M. Milligan, "The role of energy storage with renewable electricity generation," Nat. Renew. Energy Lab., Golden, CO, USA, Tech. Rep. NREL/TP-6A2-47187, Jan. 2010.
[39] P. Kundur, N. J. Balu, and M. G. Lauby, *Power System Stability and Control*. New York, NY, USA: McGraw-Hill, 1994.

YANG LI (Member, IEEE) received the B.E. degree in electrical engineering from Wuhan University, Wuhan, China, in 2007, and the M.Sc. and Ph.D. degrees in power engineering from Nanyang Technological University (NTU), Singapore, in 2008 and 2015, respectively.

From 2015 to 2016, he was a Research Fellow with the Energy Research Institute at NTU (ERI@N), Singapore. From 2016 to 2018, he was a Research Fellow with the School of Electrical Engineering and Computer Science, Queensland University of Technology, Brisbane, QLD, Australia. In 2019, he joined the School of Automation, Wuhan University of Technology, Wuhan, where he is currently an Associate Professor. His research interests include modeling and control of energy storage systems in power grid and transport sectors. He was a recipient of the EU Marie Skłodowska-Curie Action Individual Fellowship in 2020.

SAN SHING CHOI received the B.E. and Ph.D. degrees in electrical engineering from the University of Canterbury, Christchurch, New Zealand, in 1973 and 1976, respectively. He was previously with the New Zealand Electricity Department, Wellington, New Zealand, the National University of Singapore, Singapore, the State Energy Commission of Western Australia, Perth, Australia, and the Nanyang Technological University, Singapore. He is currently an Adjunct Professor with the Curtin University of Technology and the Queensland University of Technology, Brisbane, QLD, Australia. His research interests include power system control, renewable, and energy storage systems.

D. MAHINDA VILATHGAMUWA (Fellow, IEEE) received the B.Sc. degree in electrical engineering from the University of Moratuwa, Sri Lanka, in 1985, and the Ph.D. degree in electrical engineering from Cambridge University, Cambridge, U.K., in 1993.

He joined the School of Electrical and Electronic Engineering, Nanyang Technological University, Singapore, in 1993, and has served as a Faculty Member until 2013. He is currently a Professor of power engineering with the Queensland University of Technology, Brisbane, QLD, Australia. His research interests include wireless power, battery storage, power electronic converters, electrical drives, and electromobility. He has published more than 300 research papers in refereed journals and conferences, one book, and two book chapters. He has also secured two patents for his work with Rolls Royce.

BINYU XIONG (Member, IEEE) received the B.E. degree in electrical engineering from Wuhan University, Wuhan, China, in 2010, and the M.Sc. and Ph.D. degrees from Nanyang Technological University, Singapore, in 2011 and 2016, respectively. He is currently an Associate Professor with the School of Automation, Wuhan University of Technology, Wuhan. His research interests include electrical and thermal modeling of batteries, battery state of charge estimation, large-scale energy storage systems, and renewable energy generations.

JINRUI TANG (Member, IEEE) received the B.S. degree in electrical engineering from Zhejiang University, Hangzhou, China, in 2009, and the Ph.D. degree in electrical engineering from the School of Electrical and Electronic Engineering, Huazhong University of Science and Technology, Wuhan, China, in 2014. He is currently an Associate Professor with the School of Automation, Wuhan University of Technology. His research interests include distribution network protection and automation, planning, and analysis of hybrid AC/DC power system with distributed generation.